Title

Systems-informed genome mining for electroautotrophic microbial production

Authors

Anthony J. Abel,[1,†] Jacob M. Hilzinger,[2,†] Adam P. Arkin,[2,3,*] Douglas S. Clark[1,4,*]

Affiliations

1. Department of Chemical and Biomolecular Engineering, University of California, Berkeley, CA 94720, USA
2. Department of Bioengineering, University of California, Berkeley, CA 94720, USA
3. Environmental Genomics and Systems Biology Division, Lawrence Berkeley National Laboratory, 1 Cyclotron Road, Berkeley, CA 94720, USA
4. Molecular Biophysics and Integrated Bioimaging Division, Lawrence Berkeley National Laboratory, 1 Cyclotron Road, Berkeley, CA 94720, USA

[†]These authors contributed equally.
[*]Correspondence should be addressed to D.S.C. (dsc@berkeley.edu) or to A.P.A. (aparkin@lbl.gov)

Abstract

Microbial electrosynthesis (MES) systems can store renewable energy and CO_2 in many-carbon molecules inaccessible to abiotic electrochemistry. Here, we develop a multiphysics model to investigate the fundamental and practical limits of MES enabled by direct electron uptake and we identify organisms in which this biotechnological CO_2-fixation strategy can be realized. Systematic model comparisons of microbial respiration and carbon fixation strategies revealed that, under aerobic conditions, the CO_2 fixation rate is limited to <6 μmol/cm^2/hr by O_2 mass transport despite efficient electron utilization. In contrast, anaerobic nitrate respiration enables CO_2 fixation rates >50 μmol/cm^2/hr for microbes using the reductive tricarboxylic acid cycle. Phylogenetic analysis, validated by recapitulating experimental demonstrations of electroautotrophy, uncovered multiple probable electroautotrophic organisms and a significant number of genetically tractable strains that require heterologous expression of <5 proteins to gain electroautotrophic function. The model and analysis presented here will guide microbial engineering and reactor design for practical MES systems.

Main

The capture and conversion of CO_2 to fuels, commodity chemicals, and pharmaceutical precursors can help close the anthropogenic carbon cycle. Biological CO_2 fixation using plants, algae and cyanobacteria occurs naturally at scale, but biotechnological application of photosynthetic carbon fixation is challenging for several reasons including low conversion rates, low efficiencies, and difficulties with downstream separations[1]. Physicochemical strategies to fix CO_2 by generating syngas have also been considered, but extreme operating conditions and low product selectivity for complex hydrocarbons have hindered adaptation[2–4]. Recently, electromicrobial approaches, in which electrochemical reduction of CO_2 provides C_1 feedstocks to biochemical processes producing a wide array of chemicals, have been proposed[5–7]. This strategy is particularly promising because it benefits from extensive system modeling and abiotic catalyst discovery efforts[8–11]. However, poor catalyst stability, reliance on rare elements, and potential catalyst toxicity could inhibit the scalability of this method[12–14]. Microbial electrosynthesis (MES) systems may overcome these issues by obviating the need for an electrocatalyst by using so-called electroautotrophic microbes that accept electrons from a cathode via direct electron transfer (DET) mechanisms[15,16]. The inherent regenerative capacity of microbes also makes MES an attractive option for chemical production during space exploration missions because carry-along mass and materials resupply challenges are key constraints on long-term or deep-space expeditions.[17]

Despite the promise of direct MES, product spectrum and production rate bottlenecks have prevented technological realization[18]. MES systems developed to date primarily use acetogenic or methanogenic microbes that divert most of their fixed carbon into low-value acetate and methane[19]. Although genetic tools have recently become available for some of these organisms[20,21], microbial energy conservation strategies severely restrict the achievable product spectrum and selectivity. Microbes supporting electroautotrophy via the Calvin cycle have recently been discovered and are likely to alleviate product spectrum issues[22,23]. However, high throughput platforms for discovery and engineering of novel microbial chassis are in their nascent stages and distinguishing between more and less promising candidates and identifying engineering targets that enable high production rates is challenging[24,25].

Computational MES models can address this challenge by comparing microbial respiration and carbon fixation strategies. To that end, several models of MES systems have been developed, but these have assumed electron uptake interfaces directly with the intracellular NAD^+/NADH pool, in contrast to known electron transfer mechanisms[26,27]. Recent energetic calculations to determine the limiting efficiency of MES systems have addressed this issue, but assumed that aerobic respiration is equally available for all carbon fixation pathways (CFPs)[28]. Moreover, considerations of physiological mechanisms of electron transfer, respiration, and carbon fixation in models that capture relevant physical phenomena remains an outstanding challenge.

Here, we incorporate a physiological, mechanistic understanding of extracellular electron uptake into a comprehensive multiphysics model of MES that describes mass transport, electrochemical and acid-base thermodynamics and kinetics, and gas-liquid mass transfer. In the proposed mechanism, based on the reversible electron conduit in *Shewanella oneidensis*[29], electrons supplied by the cathode are split in a bifurcation scheme. A fraction is used to produce a proton motive force (PMF) via aerobic or anaerobic nitrate respiration, while the remainder is used along with the PMF to regenerate cellular energy carriers (ATP, NAD(P)H, reduced ferredoxin) consumed in the CFPs. Using this detailed picture of electron uptake, we compare the productivity and efficiency of MES systems with hypothetical microbes performing carbon fixation with each of four major CFPs and we identify physiological modules that enable the highest productivities. We further perform phylogenetic analysis of marker genes for these modules to uncover naturally occurring and/or readily engineerable microbial chassis that require the heterologous expression of only a few proteins. Thus, our analysis provides crucial insight into microbial catalyst discovery and engineering and reactor design strategies that can advance direct MES systems from basic science to technological practice.

Results

System overview. The MES model (see Computational Methods) considers a one-dimensional bioelectrochemical reactor for CO_2 reduction (Fig. 1a). The reactor has well-mixed anolyte and catholyte regions that are replenished at a fixed dilution rate and to which CO_2 is constantly supplied at a fixed partial pressure. These regions are separated by an anion exchange membrane (AEM) and fluid boundary layers, which also separate the well-mixed phases from the anode surface and the biocathode layer. The chemical species in each chamber are dissolved CO_2, dissolved O_2 (in the case of aerobic operation), bicarbonate anions (HCO_3^-), carbonate anions (CO_3^{2-}), protons (H^+), hydroxide anions (OH^-), sodium cations (Na^+), and nitrate anions (NO_3^-). The biocathode is treated as a porous electrode with microbial cells of 1-µm diameter and a porosity equivalent to that of a square lattice of spheres (Fig. 1b). We consider the physiology of direct electron transfer through the MtrCAB electron conduit (Fig. 1c) to determine the stoichiometry of CO_2 reduction to pyruvate for four major CFPs (Fig. 1d-g) using either aerobic or anaerobic nitrate respiration (Fig. 1c).

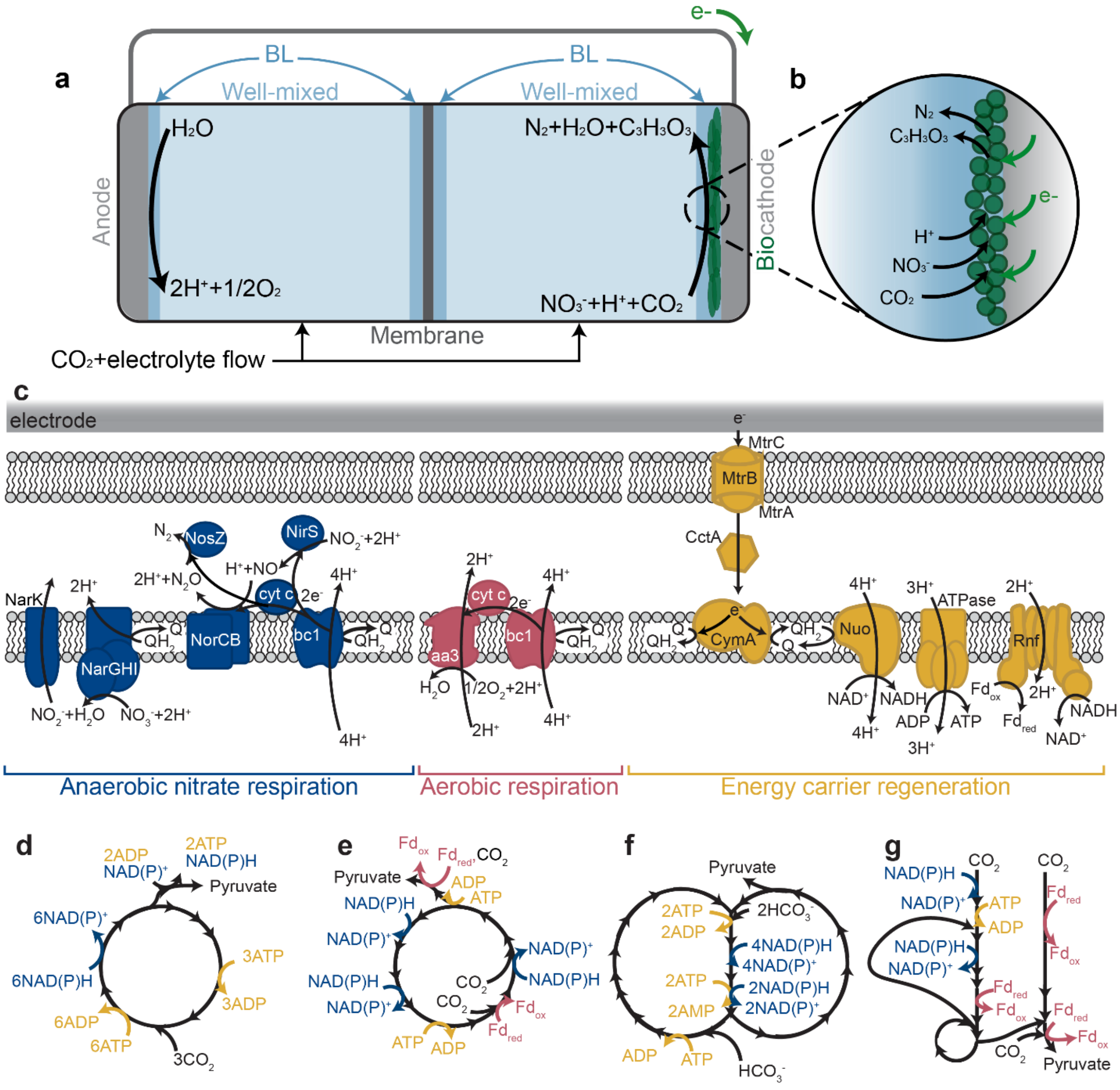
a
b
e-
BL
BL
Well-mixed
Well-mixed
Anode
H₂O
2H⁺+1/2O₂
N₂+H₂O+C₃H₃O₃
NO₃⁻+H⁺+CO₂
Biocathode
Membrane
CO₂+electrolyte flow
N₂
C₃H₃O₃
e-
H⁺
NO₃⁻
CO₂
c
electrode
e⁻
MtrC
MtrB
MtrA
CctA
NarK
2H⁺
N₂
NosZ
NirS
NO₂⁻+2H⁺
2H⁺+N₂O
H⁺+NO
4H⁺
cyt c
2e⁻
Q
QH₂
NorCB
bc1
NarGHI
NO₂⁻+H₂O
NO₃⁻+2H⁺
4H⁺
2H⁺
cyt c
2e⁻
aa3
bc1
H₂O
1/2O₂+2H⁺
2H⁺
4H⁺
CymA
Nuo
4H⁺
3H⁺
ATPase
2H⁺
Rnf
NAD⁺
NADH
ADP
ATP
Fdₒₓ
Fd_red
2H⁺
NADH
NAD⁺
4H⁺
3H⁺
Anaerobic nitrate respiration
Aerobic respiration
Energy carrier regeneration
d
2ADP
NAD(P)⁺
2ATP
NAD(P)H
Pyruvate
6NAD(P)⁺
6NAD(P)H
3ATP
3ADP
6ADP
6ATP
3CO₂
e
Fdₒₓ
Fd_red
CO₂
Pyruvate
ADP
ATP
NAD(P)H
NAD(P)⁺
NAD(P)⁺
NAD(P)H
NAD(P)H
NAD(P)⁺
CO₂
CO₂
Fdₒₓ
Fd_red
ATP
ADP
f
Pyruvate
2ATP
2ADP
2HCO₃⁻
4NAD(P)H
4NAD(P)⁺
2ATP
2AMP
2NAD(P)H
2NAD(P)⁺
ADP
ATP
HCO₃⁻
g
NAD(P)H
CO₂
CO₂
NAD(P)⁺
ATP
ADP
Fd_red
Fdₒₓ
NAD(P)H
NAD(P)⁺
Fd_red
Fdₒₓ
Fd_red
Fdₒₓ
CO₂
Pyruvate

Figure 1. Schematic of a one-dimensional microbial electrosynthesis reactor and direct electron transfer mechanisms for (an)aerobic carbon fixation. (**a**) Reactor scheme. Carbon dioxide (CO_2) and electrolyte media are fed into well-mixed regions separated by a membrane. (**b**) Direct electron transfer to a microbial biofilm supports carbon fixation to pyruvate using NO_3^- as the terminal electron acceptor. (**c**) Respiratory and energy carrier regeneration mechanisms using NO_3^- and O_2 as terminal electron acceptors. (**d**) The Calvin-Benson-Bassham (CBB), (**e**) reductive tricarboxylic acid (rTCA), (**f**) 3-hydroxypropionate bi-cycle, and (**g**) Wood-Ljungdahl pathways for carbon fixation to pyruvate shown with reducing equivalent consumption.

Comparing microbial respiration and carbon fixation pathways. The terminal electron acceptor and CFP constrain the efficiency and productivity of MES systems. Because O_2 is more electronegative than NO_3^-, aerobic respiration allows microbes to divert a higher fraction of electrons to energy carrier regeneration and therefore carbon fixation (Tables S1 and S2). For microbes using the Calvin-Benson-Bassham (CBB) cycle, aerobic respiration uses only 23.67 electrons per pyruvate molecule, while anaerobic nitrate respiration requires 61.25 electrons for the equivalent reaction. Under anaerobic conditions, obligately anaerobic CFPs use electrons more efficiently than aero-tolerant pathways: the reductive tricarboxylic acid (rTCA) cycle and the Wood-Ljungdahl pathway (WLP) require 47.5 and 46.25 electrons per pyruvate, respectively, while the CBB cycle and the 3-hydroxypropionate (3-HP) bi-cycle need 61.25 and 66.25 electrons. The rate-limiting step in carbon-fixing reactions must also be considered when evaluating productivity. While the WLP uses electrons most efficiently, the enzymatic processes are rate-limited compared to other CFPs (Table S3, Supplementary note 1), so more biomass would be needed to fix carbon at equal rates.

To determine the impacts these competing constraints have on MES systems, we calculated the pyruvate production rate as a function of O_2 partial pressure for microbes using the CBB cycle to fix carbon with O_2 as the terminal electron acceptor (Fig. 2a) and pyruvate production versus applied voltage for microbes using NO_3^- as the terminal electron acceptor and different CFPs (Fig. 2b). For aerobic respiration, pyruvate production remains <2 μmol/cm^2/hr even at O_2 partial pressures 5-fold greater than in the atmosphere (P_{O_2} = 1 atm) due mainly to the low solubility and corresponding transport limitations of O_2 in aqueous solutions (Supplementary note 2). In contrast, pyruvate production using anaerobic nitrate respiration reaches ~16.9 μmol/cm^2/hr at ~2.3 V for microbes using the rTCA cycle before the system becomes CO_2 transport limited, defined as the point at which the CO_2 concentration reaches ~0 mM at the base of the biofilm (current collector). Maximum pyruvate production rates for microbes using the CBB cycle (~7.0 μmol/cm^2/hr), 3-HP cycle (~4.4 μmol/cm^2/hr), and WLP (~1.9 μmol/cm^2/hr) are limited by the biomass available to fix carbon in 50 μm biofilms well before CO_2 transport becomes rate limiting.

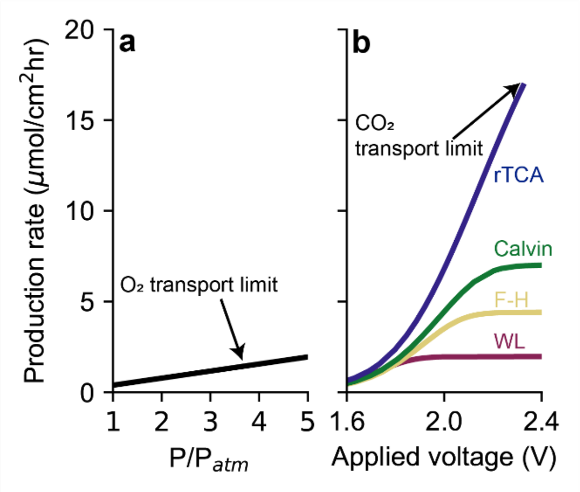

Figure 2. Effects of terminal electron acceptor and carbon fixation pathway on reactor operation. Pyruvate production rate at equivalent biofilm thickness (50 μm) as a function of (**a**) O_2 pressure supplied to the reactor headspace relative to atmospheric O_2 for microbes using the Calvin cycle with O_2 as the terminal electron acceptor, and (**b**) applied voltage for each carbon fixation pathway with NO_3^- as the terminal electron acceptor. Reactor conditions: initial pH=7.4, 0.25 M $NaNO_3$, D=5 hr^{-1}.

Biofilm thickness effects on productivity. The biofilm thickness plays an important and complex role in determining both the total carbon fixation rate and the energy efficiency of an MES system. Increasing the biofilm thickness increases the biomass available to fix carbon, enabling a higher total electron uptake rate by increasing the biomass-limited production rate. However, CO_2 transport through the biofilm will eventually impose an upper bound on the reaction rate. We plot the voltage necessary to achieve selected pyruvate production rates as a function of biofilm thickness for microbes using the rTCA cycle (Fig. 3a) or CBB cycle (Fig. 3b). For microbes using the CBB cycle, ~3.5-fold thicker biofilms are needed to achieve equivalent production rates because of the lower turnover number for the rate-limiting enzyme, RuBisCo, and the ~29% less efficient use of electrons. These factors also limit the achievable productivity of microbes using the CBB cycle to <12 μmol/cm^2/hr because thicker biofilms present a longer distance for CO_2 diffusion.

For both CFPs, increasing the biofilm thickness has a non-linear effect on the applied voltage necessary to achieve a fixed production rate (Fig. 3a, b). The initial rapid decline, and the following plateau over a wide thickness range, is due to the competing impacts of the activation overpotential for the CO_2 reduction reaction (CO_2RR) and transport-associated (Nernst and Ohmic) overpotentials (Supplementary note 3). To describe these trends, we show the applied voltage breakdown for microbes using the rTCA (Fig. 3c, d) or CBB (Fig. 3e, f) cycles at representative biofilm thicknesses. For microbes using the rTCA cycle, increasing the biofilm thickness from 35 μm (Fig. 3c) to 50 μm (Fig. 3d) increases the maximum current density the biofilm can support from ~21.5 mA/cm^2 to ~31 mA/cm^2, but CO_2 transport restricts the current density to 21.5 mA/cm^2 for the 50-μm biofilm. Increasing the biofilm thickness reduces the applied voltage necessary to achieve a given production rate (Fig. 3a). The difference is slight at lower rates because increased Ohmic loss (due to electron conduction through a thicker biofilm) mostly balances the reduced activation overpotential associated with the CO_2RR. However, as the production rate approaches the biomass-limited rate for the 35-μm film, the difference increases significantly, reaching ~200 mV at 21.5 mA/cm^2 (~16.9 μmol/cm^2/hr) because the activation overpotential for the 35-μm film rises sharply (Fig. 3c). Similar behavior is observed when comparing 50 μm (Fig. 3e) and 80 μm (Fig. 3f) biofilms using the CBB cycle to fix CO_2.

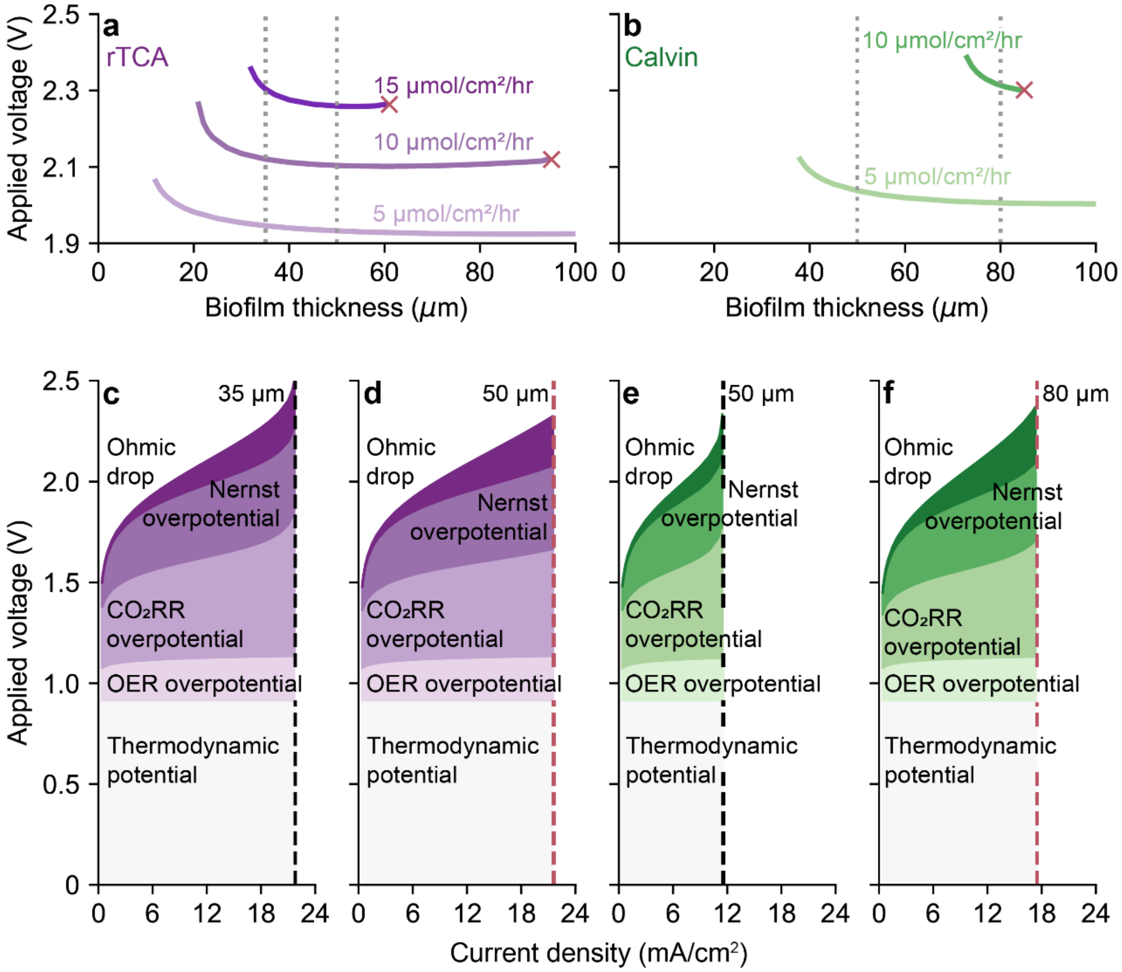

Figure 3. Effect of biofilm thickness on reactor operation. Applied voltage necessary to achieve a specific pyruvate production rate as a function of biofilm thickness for microbes fixing carbon using (**a**) the rTCA cycle and (**b**) the Calvin cycle. Applied voltage breakdown for (**c**) 35 μm, (**d**) 50 μm, (**e**) 50 μm, (**f**) 80 μm biofilms for microbes using the rTCA cycle (**c**, **d**) or Calvin cycle (**e**, **f**). Gray dotted lines in (**a**) and (**b**) correspond to biofilm thicknesses in (**c**–**f**) and were chosen to be representative of different production limits (biomass, CO_2 transport). Red crosses in (**a**, **b**) correspond to the CO_2 transport limit. Black dashed lines in (**c**, **e**) correspond to biomass-limited current density; red dashed lines in (**d**, **f**) correspond to the CO_2 transport-limited current density. Reactor conditions: initial pH=7.4, 0.25 M $NaNO_3$, D=5 hr^{-1}.

Marker gene phylogenetic analysis. Marker gene phylogeny extractions from the Reference Proteomes database resulted in a total of 5329 genomes encoding at least one marker (Fig. 4; Figs. S4-S12; Table S6). Outer membrane cytochromes and their downstream electron transfer components are modular[30,31]. Therefore, although our model focuses on MtrCAB, we extend our genome mining analysis to include other cytochromes capable of DET, including the whole MtrC/OmcA-family along with the biochemically characterized DmsE/MtrA/PioA/MtoA-, ExtA-, and Cyc2-family proteins (Supplementary note 4). We are not aware of a comprehensive multi-heme cytochrome phylogeny that contains all the clades used in this study. Here, we present this phylogeny (Fig. S11), and show the phylogenetic distribution of these cytochromes (Fig. 4).

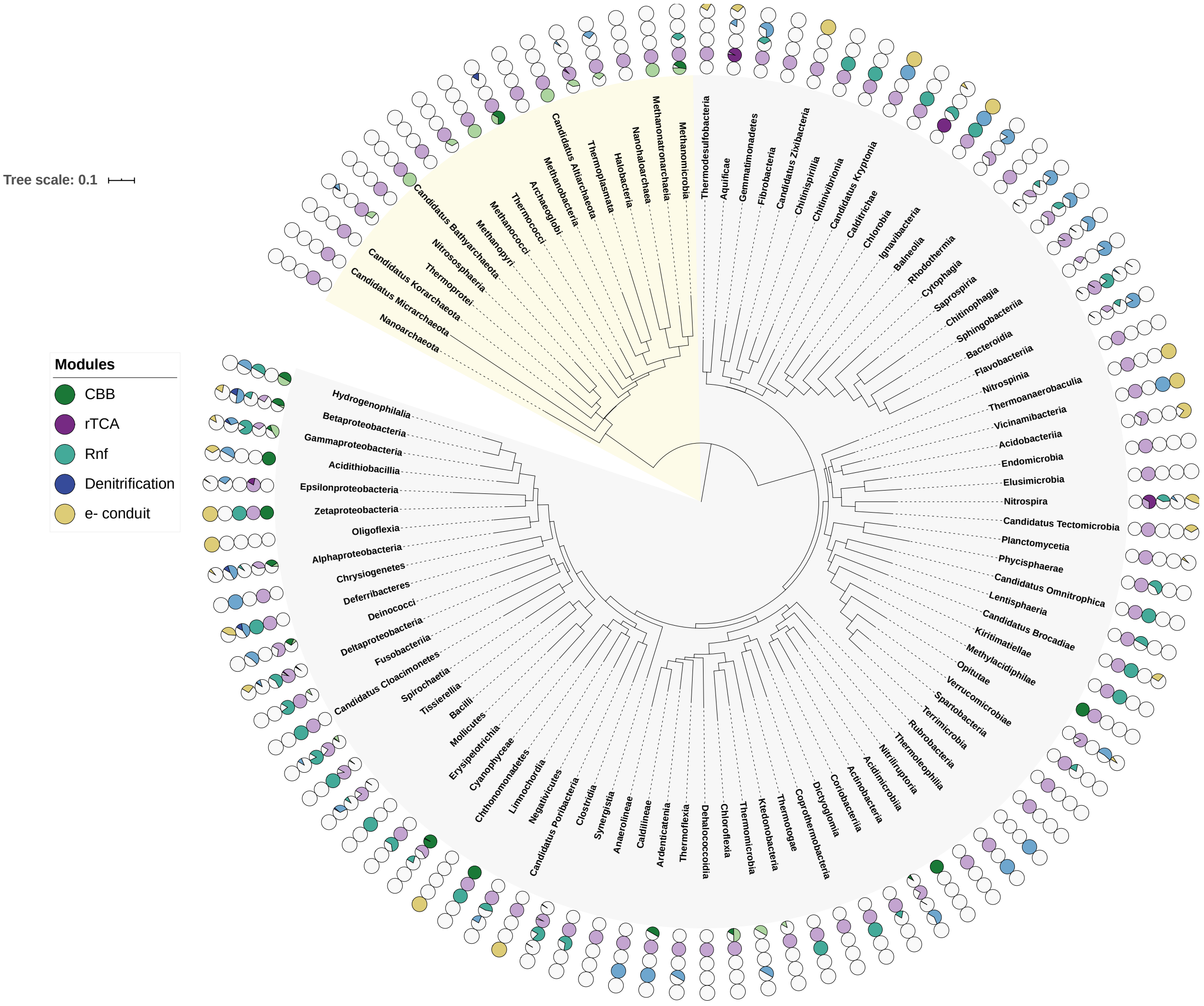

Figure 4. Distribution of target metabolic modules in the Reference Proteomes database. Species were binned by class (or phylum if no class was available), and 16S sequences representing each taxon were used to construct a phylogenetic tree. Each pie chart represents the percentage of species within each taxon that contained the appropriate marker genes. For the CBB (green), rTCA (purple), and denitrification (blue) modules, dark colors represent species that had all marker genes, while lighter colors represent species that had at least one, but not the full set of marker genes. The Rnf (teal) module represents the presence of only one marker gene, while the electron conduit (yellow) represents species that had at least one of the four possible marker genes. Archaea are highlighted in pale yellow, while bacteria are highlighted in pale gray.

We extracted 170 genomes from this dataset that have a complete CBB or rTCA cycle plus at least one electron conduit or that have promise as a chassis for engineering CBB or rTCA-based electrosynthesis (Fig. 5). Of these, 88 organisms have a complete CBB cycle plus at least one electron conduit; genetic engineering methods have been demonstrated in 17 of these organisms. Although 16 organisms have a complete rTCA cycle, only two of these organisms have genetic methods available. The remaining extracted genomes have promise as a chassis for engineering CBB- or rTCA-based electrosynthesis (Fig. 5). In total, 67 genomes encoded both PFOR and

OGOR plus at least one electron conduit but were missing AclB/CcsA. Several genomes where completion of the CBB cycle or addition of an electron conduit is feasible were also included.

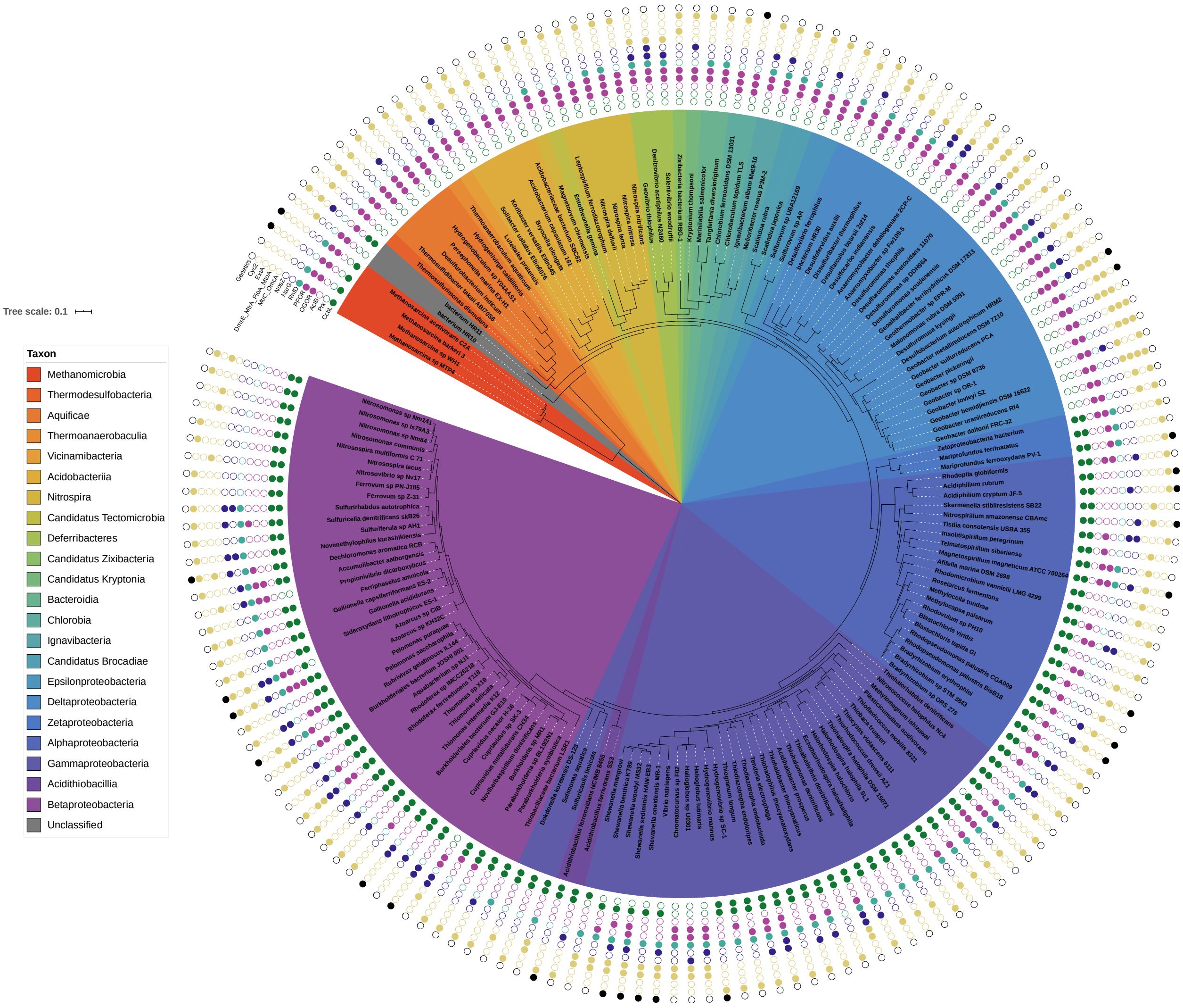
Tree scale: 0.1
Taxon
🟥 Methanomicrobia
🟧 Thermodesulfobacteria
🟧 Aquificae
🟧 Thermoanaerobaculia
🟧 Vicinamibacteria
🟨 Acidobacteriia
🟨 Nitrospira
🟩 Candidatus Tectomicrobia
🟩 Deferribacteres
🟩 Candidatus Zixibacteria
🟩 Candidatus Kryptonia
🟩 Bacteroidia
🟩 Chlorobia
🟦 Ignavibacteria
🟦 Candidatus Brocadiae
🟦 Epsilonproteobacteria
🟦 Deltaproteobacteria
🟦 Zetaproteobacteria
🟦 Alphaproteobacteria
🟪 Gammaproteobacteria
🟪 Acidithiobacillia
🟪 Betaproteobacteria
⬛ Unclassified
Genetics
Cyc2
ExtA
DmsE_MtrA_PioA_MtoA
MtrC_OmcA
NosZ
NarG
RnfD
PFOR
OGOR
AclB
Prk
CcbL

Figure 5. Species that are capable of electroautotrophy or that are potential chassis for engineering electroautotrophy. Marker gene distribution for the CBB (green) cycle, the rTCA (purple) cycle, Rnf (teal), denitrification (blue), and electron conduits (yellow) are displayed on a species-level 16S phylogenetic tree. If a given species has been genetically transformed, that species is marked as having genetics (black).

Discussion

This analysis has significant implications for MES systems. We show that although O_2 is a more efficient terminal electron acceptor than NO_3^-, low solubility severely limits the productivity of microbes using aerobic respiration. Under anaerobic nitrate respiration, the CO_2 transport limit imposes an upper bound on productivity, so increasing biofilm thicknesses cannot enable arbitrarily high production rates. For microbes with a lower enzymatic reaction rate limit (lower turnover number), the CO_2 transport limit is also lower, so microbes using the 3-HP bi-cycle and WLP cannot match the productivity achievable by microbes using the rTCA or CBB cycle regardless of the biofilm thickness. A lower turnover number for the rate-limiting enzyme also increases transport- or activation-associated overpotentials for a given CO_2-fixation rate, reducing energy efficiency. Combined, these results indicate that microbes using the rTCA cycle are likely to be both the most productive and most efficient biocatalysts for MES systems. Microbes that use the CBB cycle are the second-best option because, although the cycle's electron utilization efficiency is lower than that for the WLP, the biomass-limited reaction rate is much higher, so the CO_2 transport-limited production rate is higher and transport-associated inefficiencies are lower.

We therefore used a marker protein phylogeny-driven bioinformatics approach to identify organisms capable of electroautotrophy by coupling electron uptake to nitrate respiration and using either the CBB or rTCA cycles to fix carbon. In our dataset, 19 organisms have complete CBB cycles, NarG, and at least one electron conduit (Fig. 5). To our knowledge, none of these organisms have previously been identified as electroautotrophs and physiological confirmation plus development of genetic tools would expand the available CBB-based electroautotrophs for industrial applications. In contrast, only *Geobacter metallireducens* encodes the rTCA cycle, NarG, and at least one electron conduit. As genetic tools have been developed for *G. metallireducens*[32], this organism represents an especially promising catalyst for industrial MES. Because we identified only a small number of organisms that have all the desired modules, most of which do not have genetic tools, we also identified organisms that have potential as synthetic chassis for MES, which we discuss here in the context of several possible synthetic biology strategies for engineering electroautotrophy.

First, an organism may have a partial CFP that can be completed by heterologous expression of the missing components. Several recent demonstrations make this an attractive strategy: the CBB cycle has been engineered into heterotrophs by the addition of key enzymes[33–35], and the rTCA cycle was completed in *Geobacter sulfurreducens* to enable electroautotrophy using both rational engineering[36] and directed evolution strategies[37]. An alternate CFP, the reductive glycine pathway[38,39], is a third option since its modularity has recently been confirmed by functional expression in both *Escherichia coli*[40] and *Cupriavidus necator*[41]. Our dataset revealed several organisms in which completion of a partial CFP may be viable. Four of five *Shewanella* species identified in this study encode Prk, three encode partial rTCA cycle markers, and two encode NarG. Given the prevalence of genetic tools available to this genus, *Shewanella oneidensis*' well-characterized use in bioelectrochemical systems, and facultative anaerobic metabolism, engineering a complete CFP in *Shewanella* could lead to readily-engineerable electroautotrophs. All *Shewanella* species encode the Rnf marker gene, indicating that they can support the efficient reverse-electron transport-driven ferredoxin reduction that may be required for the rTCA cycle.

Second, an organism encoding a complete CFP may be engineered to directly uptake electrons from a cathode. The electron conduit native to *Shewanella oneidensis*, MtrCAB/CymA, has been functionally expressed in *E. coli*[42–44], which is a promising host for this strategy since multiple CFPs have been successfully engineered and it naturally respires nitrate. Alternatively, *Cupriavidus spp.* encode both a complete CBB cycle and nitrate respiration and have genetic tools available[45], making these species an attractive option for expressing an electron conduit. Because only two organisms that encode a full rTCA cycle with at least one electron conduit have genetic methods available, the green sulfur bacterium *Chlorobaculum tepidum*, which encodes the full rTCA and has genetic tools, may be another suitable host for electron conduit expression.

Finally, an organism with a complete CFP and a functional electron conduit may be engineered to use an alternate electron acceptor. We use nitrate respiration in our model since it is the most thermodynamically favorable soluble electron acceptor; nitrate respiration could be introduced in organisms by expressing the NarGHI complex. However, 5 molybdopterin cofactor biosynthesis enzymes are also necessary for proper functioning of this complex, so an appropriate chassis would benefit significantly from natural expression of these supporting proteins. *Rhodopseudomonas palustris* is an excellent candidate for this strategy since it has a characterized electron conduit[23], a complete CBB cycle, and encodes the molybdopterin biosynthesis genes. This organism has been engineered for *poly*-hydroxybutyrate[46] and *n*-butanol[47] production in MES systems, so heterologous expression of NarGHI may enable higher yields and productivities. *Azoarcus* sp. KH32C has complete CBB and rTCA cycles and encodes NosZ, while lacking NarG. A genetic system was developed in the related *Azoarcus* sp. strain BH72[48], which may open up KH32C for heterologous expression of NarGHI, further increasing the potential of this species for MES.

The multiheme cytochrome phylogeny developed here (Fig. S11) indicates that a significant number of undiscovered cytochromes that support electron exchange with an electrode may exist. This hypothesis is supported by reports of direct electron uptake independent of the four biochemically characterized families of outer membrane cytochromes used in our study: both the methanogenic archaeon *Methanosarcina barkeri*[49] and the green sulfur bacterium *Prosthecochloris aestuarii*[50] have been shown to directly accept electrons from a cathode. Cytochromes involved in direct electron transfer may therefore be more widespread and diverse than currently realized, opening the possibility of a significant number of additional chassis for MES (Supplementary note 4).

Here we have identified several microbial chassis that have potential as industrial MES strains (Table 1) and outlined a series of Technology Readiness Levels (TRLs) to evaluate industrial relevance of microbial catalysts for MES (Table S7). Beyond the genetic modules that enable electroautotrophy, additional factors constrain the productivity achievable by a given organism. For current densities >10 mA/cm^2, which are likely necessary for viable production capacity, our model predicts alkaline conditions throughout the biofilm, indicating that (facultative) alkalophilicity is a desirable trait in the ideal MES strain. A higher salinity reduces Ohmic overpotential and an increased bicarbonate concentration can enhance productivity by aiding CO_2 transport, so halophilicity or halotolerance is similarly advantageous. Unfortunately, the pH- and halo-tolerance of the organisms we identify is unclear, so future studies, in addition to confirming electroautotrophic capacity, should also characterize these traits. A suitable microbial catalyst could also be engineered to tolerate alkaline or saline conditions using rational engineering or directed evolution strategies. Because the turnover number of the rate-limiting enzyme plays a key role in setting productivity and efficiency limits for MES, these values should also be characterized in the organism(s) of interest. Strain engineering can then focus on increasing the rate limit either by increasing the enzyme turnover number or overexpressing the rate-limiting enzyme.

Table 1. Promising microbial chassis for MES

Organism	TRL†	Complete CFP	Engineered CFP
Geobacter metallireducens	1	rTCA	-
Geobacter sulfurreducens	3	-	*rTCA[36,37]
Escherichia coli	1	-	*CBB[33] and *rGly[40]
Cupriavidus necator	1	CBB	*rGly[41]
Shewanella oneidensis	1	-	rTCA or CBB
Shewanella sediminis	1	-	rTCA or CBB
Chlorobaculum tepidum	1	rTCA	-
Rhodopseudomonas palustris	4	CBB	-
Azoarcus sp. KH32C	1	rTCA and CBB	-
Methanosarcina barkeri	1	WL	rTCA or CBB
Methanosarcina acetivorans	1	WL	rTCA or CBB

†Scale: 1, least ready; 5 most ready (Table S7)
*Denotes experimental demonstration of engineered CFP

MES strain selection and engineering should also be guided by the desired product. For example, the CBB cycle is well-suited for the production of sugars such as sucrose because its end product is glyceraldehyde-3-phosphate, while the rTCA cycle may be better suited to fatty acid production since the end product, acetyl-CoA, is used directly by fatty acid biosynthesis pathways. Coupling direct electron uptake-driven carbon fixation to the biosynthesis of platform chemicals will enable a sustainable process for the conversion of CO_2 into renewable commodities.

Acknowledgements

This work was supported by the Center for the Utilization of Biological Engineering in Space (CUBES, https://cubes.space), a NASA Space Technology Research Institute (grant number NNX17AJ31G). A.J.A. is supported by an NSF Graduate Research Fellowship under grant number DGE 1752814. We thank Dr. Lien-Chun Weng (UC Berkeley) for advice on COMSOL modeling, Helen Bergstrom (UC Berkeley) for useful discussions on electrochemistry, and Dr. Paul Tol (Netherlands Institute for Space Research, SRON) for a helpful reference on accessible color schemes (https://personal.sron.nl/~pault/).

Author contributions

A.J.A. conceived of the idea, developed the model, and analyzed data. J.M.H. performed the phylogenetic analysis and analyzed data. A.J.A. and J. M. H. wrote the manuscript. A.P.A and D.S.C. edited the manuscript and supervised the project.

Competing interests

The authors have no competing interests to declare.

Data availability

Data and code used to generate figures are available at 10.6084/m9.figshare.13224617.

References

1. Blankenship, R. E. *et al.* Comparing Photosynthetic and Photovoltaic Efficiencies and Recognizing the Potential for Improvement. *Science.* **332**, 805–809 (2011).
2. Spurgeon, J. M. & Kumar, B. A comparative technoeconomic analysis of pathways for commercial electrochemical CO2 reduction to liquid products. *Energy Environ. Sci.* **11**, 1536–1551 (2018).
3. Sheng, W. *et al.* Electrochemical reduction of CO2 to synthesis gas with controlled CO/H2 ratios. *Energy Environ. Sci.* **10**, 1180–1185 (2017).
4. De Luna, P. *et al.* What would it take for renewably powered electrosynthesis to displace petrochemical processes? *Science.* **364**, (2019).
5. Yishai, O., Lindner, S. N., Gonzalez de la Cruz, J., Tenenboim, H. & Bar-Even, A. The formate bio-economy. *Curr. Opin. Chem. Biol.* **35**, 1–9 (2016).
6. Claassens, N. J., Cotton, C. A. R., Kopljar, D. & Bar-Even, A. Making quantitative sense of electromicrobial production. *Nat. Catal.* **2**, 437–447 (2019).
7. Claassens, N. J., Sánchez-Andrea, I., Sousa, D. Z. & Bar-Even, A. Towards sustainable feedstocks: A guide to electron donors for microbial carbon fixation. *Curr. Opin. Biotechnol.* **50**, 195–205 (2018).
8. Weng, L. C., Bell, A. T. & Weber, A. Z. Towards membrane-electrode assembly systems for CO2 reduction: A modeling study. *Energy Environ. Sci.* **12**, 1950–1968 (2019).
9. Weng, L. C., Bell, A. T. & Weber, A. Z. Modeling gas-diffusion electrodes for CO2 reduction. *Phys. Chem. Chem. Phys.* **20**, 16973–16984 (2018).
10. Tran, K. & Ulissi, Z. W. Active learning across intermetallics to guide discovery of electrocatalysts for CO2 reduction and H2 evolution. *Nat. Catal.* **1**, 696–703 (2018).
11. Abel, A. J. & Clark, D. S. A Comprehensive Modeling Analysis of Formate-Mediated Microbial Electrosynthesis. *ChemSusChem* 1–13 (2020). doi:10.1002/cssc.202002079
12. Chen, Y. *et al.* A Robust, Scalable Platform for the Electrochemical Conversion of CO 2 to Formate: Identifying Pathways to Higher Energy Efficiencies. *ACS Energy Lett.* **5**, 1825–1833 (2020).
13. Hegner, R., Neubert, K., Kroner, C., Holtmann, D. & Harnisch, F. Coupled Electrochemical and Microbial Catalysis for the Production of Polymer Bricks. *ChemSusChem* **13**, 5295–5300 (2020).
14. Tanaka, A. *et al.* Review of pulmonary toxicity of indium compounds to animals and humans. *Thin Solid Films* **518**, 2934–2936 (2010).
15. Grim, R. G. *et al.* Transforming the carbon economy: challenges and opportunities in the convergence of low-cost electricity and reductive CO 2 utilization. *Energy Environ. Sci.* **13**, 472–494 (2020).
16. Claassens, N. J., Sousa, D. Z., Dos Santos, V. A. P. M., De Vos, W. M. & Van Der Oost, J. Harnessing the power of microbial autotrophy. *Nat. Rev. Microbiol.* **14**, 692–706 (2016).
17. Menezes, A. A., Cumbers, J., Hogan, J. A. & Arkin, A. P. Towards synthetic biological approaches to resource utilization on space missions. *J. R. Soc. Interface* **12**, (2015).
18. Jourdin, L., Sousa, J., Stralen, N. van & Strik, D. P. B. T. B. Techno-economic assessment of microbial electrosynthesis from CO2 and/or organics: An interdisciplinary roadmap towards future research and application. *Appl. Energy* **279**, 115775 (2020).
19. Prévoteau, A., Carvajal-Arroyo, J. M., Ganigué, R. & Rabaey, K. Microbial electrosynthesis from CO2: forever a promise? *Curr. Opin. Biotechnol.* **62**, 48–57 (2020).

20. Nayak, D. D. & Metcalf, W. W. Cas9-mediated genome editing in the methanogenic archaeon Methanosarcina acetivorans. *Proc. Natl. Acad. Sci. U. S. A.* **114**, 2976–2981 (2017).
21. Leang, C., Ueki, T., Nevin, K. P. & Lovley, D. R. A Genetic system for Clostridium ljungdahlii: A chassis for autotrophic production of biocommodities and a model homoacetogen. *Appl. Environ. Microbiol.* **79**, 1102–1109 (2013).
22. Ishii, T., Kawaichi, S., Nakagawa, H., Hashimoto, K. & Nakamura, R. From chemolithoautotrophs to electrolithoautotrophs: CO2 fixation by Fe(II)-oxidizing bacteria coupled with direct uptake of electrons from solid electron sources. *Front. Microbiol.* **6**, 994 (2015).
23. Gupta, D. *et al.* Photoferrotrophs produce a PioAB electron conduit for extracellular electron uptake. *MBio* **10**, 1659–1677 (2019).
24. Yates, M. D. *et al.* Nanoliter scale electrochemistry of natural and engineered electroactive bacteria. *Bioelectrochemistry* **137**, (2021).
25. Tahernia, M. *et al.* A 96-well high-throughput, rapid-screening platform of extracellular electron transfer in microbial fuel cells. *Biosens. Bioelectron.* **162**, 112259 (2020).
26. Korth, B., Rosa, L. F. M., Harnisch, F. & Picioreanu, C. A framework for modeling electroactive microbial biofilms performing direct electron transfer. *Bioelectrochemistry* **106**, 194–206 (2015).
27. De Lichtervelde, A. C. L., Ter Heijne, A., Hamelers, H. V. M., Biesheuvel, P. M. & Dykstra, J. E. Theory of Ion and Electron Transport Coupled with Biochemical Conversions in an Electroactive Biofilm. *Phys. Rev. Appl.* **12**, 14018 (2019).
28. Salimijazi, F. *et al.* Constraints on the Efficiency of Engineered Electromicrobial Production. *Joule* **4**, 2101–2130 (2020).
29. Rowe, A. R. *et al.* Tracking electron uptake from a cathode into Shewanella cells: Implications for energy acquisition from solid-substrate electron donors. *MBio* **9**, 1–19 (2018).
30. Gupta, D., Guzman, M. S. & Bose, A. Extracellular electron uptake by autotrophic microbes: physiological, ecological, and evolutionary implications. *J. Ind. Microbiol. Biotechnol.* **47**, 863–876 (2020).
31. Conley, B. E., Weinstock, M. T., Bond, D. R. & Gralnick, J. A. A hybrid extracellular electron transfer pathway enhances the survival of vibrio natriegens. *Appl. Environ. Microbiol.* **86**, (2020).
32. Tremblay, P. L., Aklujkar, M., Leang, C., Nevin, K. P. & Lovley, D. A genetic system for Geobacter metallireducens: Role of the flagellin and pilin in the reduction of Fe(III) oxide. *Environ. Microbiol. Rep.* **4**, 82–88 (2012).
33. Gleizer, S. *et al.* Conversion of Escherichia coli to Generate All Biomass Carbon from CO2. *Cell* **179**, 1255-1263.e12 (2019).
34. Flamholz, A. I. *et al.* Functional reconstitution of a bacterial CO2 concentrating mechanism in Escherichia coli. *Elife* **9**, (2020).
35. Gassler, T. *et al.* The industrial yeast Pichia pastoris is converted from a heterotroph into an autotroph capable of growth on CO2. *Nat. Biotechnol.* **38**, 210–216 (2020).
36. Ueki, T. *et al.* Construction of a geobacter strain with exceptional growth on cathodes. *Front. Microbiol.* **9**, 1512 (2018).
37. Zhang, T., Shi, X. C., Ding, R., Xu, K. & Tremblay, P. L. The hidden chemolithoautotrophic metabolism of Geobacter sulfurreducens uncovered by adaptation

to formate. *ISME J.* **14**, 2078–2089 (2020).

38. Bar-Even, A., Noor, E., Flamholz, A. & Milo, R. Design and analysis of metabolic pathways supporting formatotrophic growth for electricity-dependent cultivation of microbes. *Biochim. Biophys. Acta - Bioenerg.* **1827**, 1039–1047 (2013).
39. Sánchez-Andrea, I. *et al.* The reductive glycine pathway allows autotrophic growth of Desulfovibrio desulfuricans. *Nat. Commun.* 1–12 (2020). doi:10.1038/s41467-020-18906-7
40. Kim, S. *et al.* Growth of E. coli on formate and methanol via the reductive glycine pathway. *Nat. Chem. Biol.* **16**, 538–545 (2020).
41. Claassens, N. J. *et al.* Replacing the Calvin cycle with the reductive glycine pathway in Cupriavidus necator. *Metab. Eng.* **62**, 30–41 (2020).
42. Jensen, H. M. *et al.* Engineering of a synthetic electron conduit in living cells. *Proc. Natl. Acad. Sci.* **107**, 19213–19218 (2010).
43. Jensen, H. M., TerAvest, M. A., Kokish, M. G. & Ajo-Franklin, C. M. CymA and Exogenous Flavins Improve Extracellular Electron Transfer and Couple It to Cell Growth in Mtr-Expressing Escherichia coli. *ACS Synth. Biol.* **5**, 679–688 (2016).
44. Coursolle, D. & Gralnick, J. A. Modularity of the mtr respiratory pathway of shewanella oneidensis strain MR-1. *Mol. Microbiol.* **77**, 995–1008 (2010).
45. Bi, C. *et al.* Development of a broad-host synthetic biology toolbox for ralstonia eutropha and its application to engineering hydrocarbon biofuel production. *Microb. Cell Fact.* **12**, 1–10 (2013).
46. Ranaivoarisoa, T. O., Singh, R., Rengasamy, K., Guzman, M. S. & Bose, A. Towards sustainable bioplastic production using the photoautotrophic bacterium Rhodopseudomonas palustris TIE-1. *J. Ind. Microbiol. Biotechnol.* **46**, 1401–1417 (2019).
47. Bai, W., Ranaivoarisoa, T. O., Singh, R., Rengasamy, K. & Bose, A. Sustainable Production of the Biofuel n-Butanol by Rhodopseudomonas palustris TIE-1. *bioRxiv* (2020). doi:10.1101/2020.10.13.336636
48. Böhm, M., Hurek, T. & Reinhold-Hurek, B. Twitching motility is essential for endophytic rice colonization by the N2-fixing endophyte Azoarcus sp. strain BH72. *Mol. Plant-Microbe Interact.* **20**, 526–533 (2007).
49. Rowe, A. R. *et al.* Methane-Linked Mechanisms of Electron Uptake from Cathodes by Methanosarcina barkeri. *MBio* **10**, (2019).
50. Ha, P. T. *et al.* Syntrophic anaerobic photosynthesis via direct interspecies electron transfer. *Nat. Commun.* **8**, 1–7 (2017).

Computational Methods

System overview. Species transport for an open electrochemical system must satisfy mass conservation:

$$\frac{\partial c_i}{\partial t} + \frac{\partial N_i}{\partial x} = R_{\mathrm{F},i} + R_{\mathrm{H},i} + R_{\mathrm{CT},i} \qquad (1)$$

where c_i is the concentration, N_i is the molar flux, and $R_{\mathrm{F},i}$, $R_{\mathrm{H},i}$, and $R_{\mathrm{CT},i}$ are the net volumetric rates of formation or consumption for species i (CO_2, HCO_3^-, CO_3^{2-}, H^+, OH^-, Na^+, NO_3^-) due to gas and electrolyte (F) feed terms, homogeneous (H) chemical reactions, and electrochemical charge transfer (CT) reactions, respectively. $R_{\mathrm{F},i}$ applies only in the well-mixed electrolyte phases where gas and electrolyte feeds are introduced and $R_{\mathrm{CT},i}$ applies only in the porous biocathode layer.

In the following sections, we formulate the equations that govern transport and reactions within the MES system, describe assumptions, and report the key parameter values used in our model.

Species transport in the electrolyte boundary layers, membrane, and porous biocathode. The molar flux of species (assuming no net fluid velocity) in dilute electrolyte solutions is written as the sum of diffusive and migrative fluxes:

$$N_i = -D_i \frac{\partial c_i}{\partial x} - z_i u_i F c_i \frac{\partial \phi_\mathrm{l}}{\partial x} \tag{2}$$

where D_i and u_i are the diffusivity and mobility (related by the Nernst-Einstein relationship, $u_i = D_i/RT$ for dilute solutions) of species i, z_i is the charge number, F is Faraday's constant, and ϕ_l is the local electrolyte potential. In the anion exchange membrane (AEM), we reduce diffusion coefficients of anions and cations by a factor of 10 and 100 respectively relative to those in the electrolyte to model a generic anion exchange membrane and assume a fixed background positive unit charge with a 0.5 M concentration, following Singh *et al.*[1] We also use effective diffusion coefficients within the biocathode layer calculated using the Bruggeman relationship,

$$D_{i,\mathrm{eff}} = {\epsilon_\mathrm{p}}^{3/2} D_i \tag{3}$$

where ϵ_p is the biofilm porosity. The net ionic current density in the electrolyte (i_l) can be calculated from the total ionic flux:

$$i_\mathrm{l} = F \sum_i z_i N_i \tag{4}$$

where F is Faraday's constant and z_i is the charge number, following electroneutrality,

$$\sum_i z_i c_i = 0 \tag{5}$$

Gas feed and electrolyte flow in the well-mixed electrolyte. The well-mixed electrolyte regions are assumed to have sufficient convective mixing such that no concentration gradients are formed. Species transport into and out of the boundary layers is considered at the interface between the well-mixed and boundary layer electrolyte phases (Fig. 1a, b). Constant gas feed and electrolyte flow terms in the well-mixed regions are included to describe a continuously operating system, given by:

$$R_{\mathrm{F,CO_2}} = k_\mathrm{L} a \left(K_0 P_{\mathrm{CO_2}} - c_{\mathrm{CO_2}} \right) \tag{6}$$

$$R_{\mathrm{F},i\neq \mathrm{CO_2}} = D\left(c_{i,0} - c_i\right) \tag{7}$$

where $k_\mathrm{L}a$ is the volumetric mass-transfer coefficient (in units s^{-1}) on the liquid side of the gas/liquid interface, K_0 is Henry's constant for CO_2 in water, $P_{\mathrm{CO_2}}$ is the pressure of CO_2 in the gas phase, D is the dilution rate (defined as the inverse space time, or volumetric flow rate divided by reactor volume), and $c_{i,0}$ is the initial or feed concentration of the ith species. The equilibrium of CO_2 between the gas and liquid phases, $\mathrm{CO_2}_{(\mathrm{g})} \leftrightarrow \mathrm{CO_2}_{(\mathrm{aq})}$, is described by Henry's constant such that:

$$K_0 = \frac{c_{\mathrm{CO_2}}}{P_{\mathrm{CO_2}}} \tag{8}$$

Henry's constant for CO_2 depends on the temperature and salinity of the aqueous phase and follows an empirical relationship[2],

$$\begin{gathered}\ln(K_0) = 93.4517\left(\frac{100}{T}\right) - 60.2409 + 23.3585 \ln\left(\frac{T}{100}\right) + \\ S\left(0.023517 - 0.023656\left(\frac{T}{100}\right) + 0.0047036\left(\frac{T}{100}\right)^2\right)\end{gathered} \tag{9}$$

where S is the salinity in units g/kg and T is the temperature.

Homogeneous chemical reactions. The acid-base bicarbonate/carbonate and water-dissociation reactions shown below occur in all phases and are treated as kinetic expressions without assuming equilibrium (eq. 15):

$$\mathrm{CO_2}_{(\mathrm{aq})} + \mathrm{H_2O} \xleftrightarrow{k_{+1},k_{-1}} \mathrm{H^+} + \mathrm{HCO_3}^- \qquad K_1 \tag{10}$$

$$\mathrm{HCO_3}^- \xleftrightarrow{k_{+2},k_{-2}} \mathrm{H^+} + \mathrm{CO_3}^{2-} \qquad K_2 \tag{11}$$

$$\mathrm{CO_2}_{(\mathrm{aq})} + \mathrm{OH^-} \xleftrightarrow{k_{+3},k_{-3}} \mathrm{HCO_3}^- \qquad K_3 = K_1/K_\mathrm{w} \tag{12}$$

$$\mathrm{HCO_3}^- + OH^- \xleftrightarrow{k_{+4},k_{-4}} \mathrm{CO_3}^{2-} + \mathrm{H_2O} \qquad K_4 = K_2/K_\mathrm{w} \tag{13}$$

$$\mathrm{H_2O} \xleftrightarrow{k_\mathrm{w},k_{-\mathrm{w}}} \mathrm{H^+} + \mathrm{OH^-} \qquad K_\mathrm{W} \tag{14}$$

where k_{+n} and k_{-n} are the forward and reverse rate constants, respectively, and K_n is the equilibrium constant for the nth reaction. Source and sink terms resulting from these reactions are compiled in $R_{\mathrm{H},i}$, written as:

$$R_{\mathrm{H},i} = \sum_n \nu_i \left(k_{+n} \prod_{\nu_i<0} c_i - k_{-n} \prod_{\nu_i>0} c_i \right) \tag{15}$$

where ν_i is the stoichiometric coefficient of species i for the nth reaction and reverse rate constants are calculated from:

$$k_{-n} = \frac{k_{+n}}{K_n} \qquad (16)$$

Electrode reactions – anode. The surface reaction at the anode is the oxidation of water:

$$\mathrm{H_2O} \longrightarrow \frac{1}{2}\mathrm{O_2} + 2\mathrm{H^+} + 2\mathrm{e^-} \qquad E^0_{\mathrm{OER}} \qquad (17)$$

where E^0_{OER} is the equilibrium potential of the oxygen evolution half-cell reaction (OER) at standard state. The anode reaction is related to species transport by a flux boundary condition at the electrode surface,

$$N_i = \frac{-\nu_i i_{\mathrm{R}}}{nF} \qquad (18)$$

where i_{R} is the reaction current density and n is the number of electrons participating in the electrode reaction. We model charge transfer kinetics at the anode using Butler-Volmer kinetics:

$$i_{\mathrm{R}} = i_0 \left[\left(\frac{c_{\mathrm{red}}}{c_{\mathrm{red,0}}} \right)^{\gamma_{\mathrm{red}}} \exp\left(\frac{\alpha_{\mathrm{a}} F \eta}{RT} \right) - \left(\frac{c_{\mathrm{ox}}}{c_{\mathrm{ox,0}}} \right)^{\gamma_{\mathrm{ox}}} \exp\left(\frac{\alpha_{\mathrm{c}} F \eta}{RT} \right) \right] \qquad (19)$$

where i_0 is the constant exchange current density, $\gamma_{\mathrm{red/ox}}$ is the reaction order with respect to a reactant, $\alpha_{\mathrm{a/c}}$ is the anodic/cathodic transfer coefficient, and η is the overpotential. The overpotential is defined according to:

$$\eta = \phi_{\mathrm{s}} - \phi_{\mathrm{l}} - E \qquad (20)$$

where ϕ_{s} is the electrode potential, ϕ_{l} is the electrolyte potential, and E is the half-cell equilibrium potential.

Because water oxidation creates acidic conditions near the anode surface, bicarbonate and carbonate species will be converted to aqueous CO_2 according to Le Chatelier’s principle. To avoid the unrealistic supersaturation of CO_2 in the electrolyte this would cause, we describe evolution of CO_2 in the electrolyte (Supplementary note 6) as:

$$\begin{aligned} R_{\mathrm{CO_2,evolution}} &= -\gamma \left(\frac{c_{\mathrm{CO_2}}}{K_0 f_{\mathrm{CO_2}}} \right)^2 & \frac{c_{\mathrm{CO_2}}}{K_0 P_{\mathrm{CO_2}}} > 1 \\ &= 0 & \frac{c_{\mathrm{CO_2}}}{K_0 P_{\mathrm{CO_2}}} \le 1 \end{aligned} \qquad (21)$$

where γ is the releasing coefficient and $c_{\mathrm{CO_2}}/K_0 P_{\mathrm{CO_2}}$ is the supersaturation ratio. This formulation was originally reported by Wilt, and was utilized to describe CO_2 evolution in abiotic electrochemical systems previously[1,3–5].

Electrode reactions – biocathode. We consider the physiology of direct electron transfer through the MtrCAB electron conduit (Fig. 1c in the main text) to determine the stoichiometry of CO_2 reduction to pyruvate for four major carbon fixation pathways (Fig. 1d–g in the main text) using either aerobic or anaerobic nitrate respiration. All processes start with quinone (Q) reduction,

$$\mathrm{Q} + 2\mathrm{H^+}_{\mathrm{in}} + 2\mathrm{e^-} \rightarrow \mathrm{QH_2} \qquad (22)$$

using the MtrCAB/CctA/CymA electron conduit native to *S. oneidensis*[6–9]. For aerobic respiration, the respiratory complex III (*e.g.* the *bc1* complex) oxidizes a quinol, pumping protons across the inner membrane[10,11]:

$$\mathrm{QH_2} + 2\mathrm{H^+}_{\mathrm{in}} \rightarrow \mathrm{Q} + 4\mathrm{H^+}_{\mathrm{out}} + 2\mathrm{e^-} \qquad (23)$$

where the subscripts “in” and “out” refer to ion locations in the intracellular space and periplasm, respectively. The two electrons liberated in this process are transported by *c*-type cytochromes to respiratory complex IV (*e.g.* the *aa3* complex), which transports two additional protons across the inner membrane and reduces O_2 to H_2O[10,12]:

$$\frac{1}{2}\mathrm{O_2} + 2\mathrm{H^+} + 2\mathrm{e^-} + 2\mathrm{H^+}_{\mathrm{in}} \rightarrow \mathrm{H_2O} + 2\mathrm{H^+}_{\mathrm{out}} \qquad (24)$$

For anaerobic nitrate respiration, quinols are consumed both to pump protons via respiratory complex III, eq. (23), and to reduce NO_3^- to nitrite (NO_2^-) using, *e.g.* the Nar complex[13]:

$$\mathrm{NO_3}^- + 2\mathrm{H^+} + \mathrm{QH_2} \rightarrow \mathrm{NO_2}^- + \mathrm{H_2O} + \mathrm{Q} + 2\mathrm{H^+}_{\mathrm{out}} \qquad (25)$$

Further reactions consume electrons liberated by quinol oxidation to complete the reduction of NO_2^- to N_2[13]:

$$\mathrm{NO_2}^- + 2\mathrm{H^+} + \mathrm{e^-} \rightarrow \mathrm{NO} + \mathrm{H_2O} \qquad (26)$$

$$\mathrm{NO} + \mathrm{H^+} + \mathrm{e^-} \rightarrow \frac{1}{2}\mathrm{N_2O} + \frac{1}{2}\mathrm{H_2O} \qquad (27)$$

$$\mathrm{N_2O} + 2\mathrm{H^+} + 2\mathrm{e^-} \rightarrow \mathrm{N_2} + \mathrm{H_2O} \qquad (28)$$

Carbon fixation pathways require NAD(P)H, ATP, and/or reduced ferredoxins (Fd_{red}) as reducing equivalents[14]. Cells can regenerate these reducing equivalents by translocating protons (PMF consumption) using, *e.g.*, the Nuo complex for NADH[15], ATP synthase for ATP[16], and the Rnf complex for ferredoxins[17–19] according to:

$$\mathrm{NAD^+} + 4\mathrm{H^+}_{\mathrm{out}} + \mathrm{QH_2} \rightarrow \mathrm{NADH} + 4\mathrm{H^+}_{\mathrm{in}} + \mathrm{Q} \qquad (29)$$

$$\mathrm{ADP} + 3\mathrm{H^+}_{\mathrm{out}} \rightarrow \mathrm{ATP} + 3\mathrm{H^+}_{\mathrm{in}} \tag{30}$$

$$\mathrm{Fd_{ox}} + \mathrm{NADH} + 2\mathrm{H^+}_{\mathrm{out}} \rightarrow \mathrm{Fd_{red}} + \mathrm{NAD^+} + 2\mathrm{H^+}_{\mathrm{in}} \tag{31}$$

We use these regeneration mechanisms to determine the stoichiometry (number of reduced molecules produced per number of electrons consumed) for aerobic or anaerobic nitrate respiration (Table S1). Because carbon fixation pathways have different energy carrier requirements, we also derive the overall stoichiometry for CO_2 reduction to pyruvic acid (pyruvate) (Table S2). For the aero-tolerant carbon fixation pathways (Calvin cycle, eq. (32), Fuchs-Holo bi-cycle, eq. (33)), the cathodic half-cell reactions using aerobic respiration are:

$$3\mathrm{CO_2} + 3\frac{5}{12}\mathrm{O_2} + 23\frac{2}{3}\mathrm{H^+} + 23\frac{2}{3}\mathrm{e^-} \rightarrow \mathrm{C_3H_4O_3} + 9\frac{5}{6}\mathrm{H_2O} \tag{32}$$

$$3\mathrm{CO_2} + 3\frac{3}{4}\mathrm{O_2} + 25\mathrm{H^+} + 25\mathrm{e^-} \rightarrow \mathrm{C_3H_4O_3} + 10\frac{1}{2}\mathrm{H_2O} \tag{33}$$

For carbon fixation pathways using NO_3^- as the terminal electron acceptor, the half-cell reactions are:

$$\begin{aligned} &3\mathrm{CO_2} + 10\frac{1}{4}\mathrm{NO_3}^- + 71\frac{1}{2}\mathrm{H^+} + 61\frac{1}{4}\mathrm{e^-} \\ &\qquad \rightarrow \mathrm{C_3H_4O_3} + 5\frac{1}{8}\mathrm{N_2} + 33\frac{3}{4}\mathrm{H_2O} \end{aligned} \tag{34}$$

$$\begin{aligned} &3\mathrm{CO_2} + 7\frac{1}{2}\mathrm{NO_3}^- + 55\mathrm{H^+} + 47\frac{1}{2}\mathrm{e^-} \\ &\qquad \rightarrow \mathrm{C_3H_4O_3} + 3\frac{1}{4}\mathrm{N_2} + 25\frac{1}{2}\mathrm{H_2O} \end{aligned} \tag{35}$$

$$\begin{aligned} &3\mathrm{CO_2} + 11\frac{1}{4}\mathrm{NO_3}^- + 77\frac{1}{2}\mathrm{H^+} + 66\frac{1}{4}\mathrm{e^-} \\ &\qquad \rightarrow \mathrm{C_3H_4O_3} + 5\frac{5}{8}\mathrm{N_2} + 36\frac{3}{4}\mathrm{H_2O} \end{aligned} \tag{36}$$

$$\begin{aligned} &3\mathrm{CO_2} + 7\frac{1}{4}\mathrm{NO_3}^- + 53\frac{1}{2}\mathrm{H^+} + 46\frac{1}{4}\mathrm{e^-} \\ &\qquad \rightarrow \mathrm{C_3H_4O_3} + 3\frac{1}{8}\mathrm{N_2} + 24\frac{3}{4}\mathrm{H_2O} \end{aligned} \tag{37}$$

where eq. (34) is for the Calvin cycle, eq. (35) is for the rTCA cycle, eq. (36) is for the Fuchs-Holo bicycle (F-H), and eq. (37) is for the Wood-Ljungdahl (WL) pathway.

Biocathode reactions, eq. (32–37), relate CO_2-fixing reactions to species transport in the biocathode layer by,

$$R_{\mathrm{CT},i} = \frac{\nu_i a_\mathrm{v} i_\mathrm{B}}{nF} \tag{38}$$

where a_v is the active specific surface area of the biocathode and i_B is the current density on the biocathode surfaces. The active specific surface area is calculated based on the geometric assumptions described above, resulting in:

$$a_\mathrm{v} = \frac{3\left(1 - \epsilon_\mathrm{p}\right)}{r_\mathrm{cell}} \tag{39}$$

where r_cell is the radius of the spherical microbe. The current density can be limited by the maximum rate at which the cells can fix CO_2, which depends on the turnover number of the rate-limiting enzyme in the carbon fixation pathway. To account for this, we impose a limit on i_B via:

$$i_\mathrm{B} = \frac{i_\mathrm{R}}{1 + \left|\frac{i_\mathrm{R}}{i_\mathrm{lim}}\right|} \tag{40}$$

where i_lim is the biomass-limited current density. We calculate the biomass-limited current density by projecting the enzymatic rate limit to the total cell surface:

$$i_\mathrm{lim} = nFk_\mathrm{cat}\left(\frac{n_\mathrm{E}}{N_\mathrm{Av}V_\mathrm{cell}}\right)\left(\frac{1 - \epsilon_\mathrm{p}}{a_\mathrm{v}}\right) \tag{41}$$

where k_cat is the enzyme turnover number (units s^{-1}), n_E is the enzyme amount in each cell (units $cell^{-1}$) N_Av is Avogadro's number, and V_cell is the microbe volume. This formulation for the limiting current density relies on the fact that the rate of intracellular diffusion of substrates is much faster than the rate-limiting reaction step in carbon fixation pathways (see supplementary note 5 for calculations), indicating that energy carriers and CO_2 have complete and effectively immediate access to intracellular enzymes once generated at or delivered to the cell surface. We model charge transfer using Butler-Volmer kinetics, eq. (19).

Electron transport in the solid electrode. Electron transport in the solid electrode regions is governed by charge conservation and Ohm's law, given by:

$$\nabla i_\mathrm{s} = -\nabla i_\mathrm{l} = -a_\mathrm{v} i_\mathrm{B} \tag{42}$$

$$i_\mathrm{s} = \kappa_\mathrm{s} \frac{\partial \phi_\mathrm{s}}{\partial x} \tag{43}$$

where i_s is the electrode current density and κ_s is the anode/biocathode conductivity. The conductivity in the biocathode is modified by a Bruggeman correction:

$$\kappa_{s,\mathrm{eff}} = (1 - \epsilon_\mathrm{p})^{1.5} \kappa_\mathrm{s} \tag{44}$$

Numerical method. The governing equations are solved using the MUMPS general solver in COMSOL Multiphysics 5.4. The modeling domain has a maximum element size of 10 μm in the well-mixed regions and 0.5 μm near boundaries to capture steep concentration gradients; the solution was independent of increasing mesh resolution. Model parameters are listed in Table 3. The potential in the reactor is calculated relative to zero potential at the cathode base and potential or current density is applied as a boundary condition at the anode.

Construction and analysis of phylogenetic trees. Seed sequences for marker genes[20–22] of each pathway (Table S4) were fed to JackHMMER for homology searches[23]. Protein identifiers from the JackHMMER output were used to retrieve full-length protein sequences from Uniprot (The Uniprot Consortium 2019). Protein alignments were created using MAFTT[24,25]. Maximum likelihood trees for each protein search result were built using FastTree 2[26]. Trees were visualized with Iroki[27]. Trees were manually annotated through a combination of conserved protein domain information (The Uniprot Consortium 2019), inclusion of characterized proteins when available[28,29], and nearest characterized protein information for uncharacterized proteins[29]. Protein sequences corresponding to each marker gene were extracted from the phylogenies using the R package ape[30]. Extracted protein sequences for all marker genes were used to construct a table containing gene presence or absence information for each genome in the dataset (Table S6). Phylogenetic trees displaying gene presence and absence data were built using 16S sequences that were aligned using MAFFT[24,25], built using FastTree 2[26], and visualized using the Interactive Tree of Life[31] and annotated using taxonomy data from NCBI. Presence of genetic tools was established through a literature search (Table S5).

MtrC from *Shewanella oneidensis* was used as the seed sequence in generating the multi-heme cytochrome phylogeny (Table S4). The JackHMMER output was filtered to exclude sequences with less than eight heme motifs (CxxCH or CxxxCH), and those sequences outside the range of sequence lengths of sequences containing exactly ten heme motifs (188-1434 amino acids). Biochemically characterized multi-heme cytochromes were used to annotate the phylogeny: MtrC[32], OmcA[33], MtrF[33], PioA[34,35], MtoA[36], DmsE[37], MtrA[33], MtrD[33], and ExtA[38]. Although MtrA/D are components of three-subunit electron conduits with MtrC/F, members of this clade, such as PioA and MtoA, are components of two-subunit electron conduits. While DmsE is characterized as being a DMSO reductase, this protein clustered very closely to MtrA and MtrD, and we were therefore unable to separate putative DMSO reductases from cytochromes that may interact with an electrode. Thus, all members of the DmsE/MtrA/PioA/MtoA-family clade of proteins were kept for downstream analysis as potential multi-heme cytochromes involved in direct electron transfer with an electrode.

Computational Methods References

51. Singh, M. R., Clark, E. L. & Bell, A. T. Effects of electrolyte, catalyst, and membrane composition and operating conditions on the performance of solar-driven electrochemical reduction of carbon dioxide. *Phys. Chem. Chem. Phys.* **17**, 18924–18936 (2015).
52. Ulf Riebesell, Victoria J. Fabry, Lina Hansson & Jean-Pierre Gattuso. *Guide to best practices for ocean acidification research and data reporting*. *Publications Office of the European Union Luxembourg* (2011). doi:10.2777/66906
53. Wilt, P. M. Nucleation rates and bubble stability in water-carbon dioxide solutions. *J. Colloid Interface Sci.* **112**, 530–538 (1986).
54. Lin, M., Han, L., Singh, M. R. & Xiang, C. An Experimental- And Simulation-Based

Evaluation of the CO2 Utilization Efficiency of Aqueous-Based Electrochemical CO2 Reduction Reactors with Ion-Selective Membranes. *ACS Appl. Energy Mater.* **2**, 5843–5850 (2019).

55. Abel, A. J. & Clark, D. S. A Comprehensive Modeling Analysis of Formate-Mediated Microbial Electrosynthesis. *ChemSusChem* 1–13 (2020). doi:10.1002/cssc.202002079
56. Rowe, A. R. *et al.* Tracking electron uptake from a cathode into Shewanella cells: Implications for energy acquisition from solid-substrate electron donors. *MBio* **9**, 1–19 (2018).
57. Alves, M. N. *et al.* Characterization of the periplasmic redox network that sustains the versatile anaerobic metabolism of Shewanella oneidensis MR-1. *Front. Microbiol.* **6**, 665 (2015).
58. Kracke, F., Vassilev, I. & Krömer, J. O. Microbial electron transport and energy conservation - The foundation for optimizing bioelectrochemical systems. *Front. Microbiol.* **6**, 1–18 (2015).
59. Ross, D. E., Flynn, J. M., Baron, D. B., Gralnick, J. A. & Bond, D. R. Towards electrosynthesis in Shewanella: Energetics of reversing the Mtr pathway for reductive metabolism. *PLoS One* **6**, (2011).
60. Mitchell, P. Possible molecular mechanisms of the protonmotive function of cytochrome systems. *J. Theor. Biol.* **62**, 327–367 (1976).
61. Lange, C. & Hunte, C. Crystal structure of the yeast cytochrome bc1 complex with its bound substrate cytochrome c. *Proc. Natl. Acad. Sci. U. S. A.* **99**, 2800–2805 (2002).
62. Saraste, M. Oxidative phosphorylation at the fin de siecle. *Science (80-.).* **283**, 1488–1493 (1999).
63. Moreno-Vivián, C., Cabello, P., Martínez-Luque, M., Blasco, R. & Castillo, F. Prokaryotic nitrate reduction: Molecular properties and functional distinction among bacterial nitrate reductases. *J. Bacteriol.* **181**, 6573–6584 (1999).
64. Berg, I. A. Ecological Aspects of the Distribution of Different Autotrophic CO 2 Fixation Pathways. *Appl. Environ. Microbiol.* **77**, 1925–1936 (2011).
65. Yagi, T. The bacterial energy-transducing NADH-quinone oxidoreductases. *Biochim. Biophys. Acta - Bioenerg.* **1141**, 1–17 (1993).
66. Mitchell, P. Chemiosmotic coupling in oxidative and photosynthetic phosphorylation. *Biol. Rev. Camb. Philos. Soc.* **41**, 445–502 (1966).
67. Biegel, E., Schmidt, S., González, J. M. & Müller, V. Biochemistry, evolution and physiological function of the Rnf complex, a novel ion-motive electron transport complex in prokaryotes. *Cell. Mol. Life Sci.* **68**, 613–634 (2011).
68. Tremblay, P. L., Zhang, T., Dar, S. A., Leang, C. & Lovley, D. R. The Rnf complex of Clostridium ljungdahlii is a proton-translocating ferredoxin: NAD+ oxidoreductase essential for autotrophic growth. *MBio* **4**, (2013).
69. Rubin-Blum, M., Dubilier, N. & Kleiner, M. Genetic Evidence for Two Carbon Fixation Pathways (the Calvin-Benson-Bassham Cycle and the Reverse Tricarboxylic Acid Cycle) in Symbiotic and Free-Living Bacteria. *mSphere* **4**, (2019).
70. Campbell, B. J. & Gary, S. C. Abundance of reverse tricarboxylic acid cycle genes in free-living microorganisms at deep-sea hydrothermal vents. *Appl. Environ. Microbiol.* **70**, 6282–6289 (2004).
71. Kandeler, E., Deiglmayr, K., Tscherko, D., Bru, D. & Philippot, L. Abundance of narG, nirS, nirK, and nosZ genes of denitrifying bacteria during primary successions of a glacier

foreland. *Appl. Environ. Microbiol.* **72**, 5957–5962 (2006).
72. Hügler, M. & Sievert, S. M. Beyond the Calvin Cycle: Autotrophic Carbon Fixation in the Ocean. *Ann. Rev. Mar. Sci.* **3**, 261–289 (2011).
73. Johnson, L. S., Eddy, S. R. & Portugaly, E. Hidden Markov model speed heuristic and iterative HMM search procedure. *BMC Bioinformatics* **11**, (2010).
74. Katoh, K. & Standley, D. M. MAFFT multiple sequence alignment software version 7: Improvements in performance and usability. *Mol. Biol. Evol.* **30**, 772–780 (2013).
75. Katoh, K., Rozewicki, J. & Yamada, K. D. MAFFT online service: Multiple sequence alignment, interactive sequence choice and visualization. *Brief. Bioinform.* **20**, 1160–1166 (2018).
76. Price, M. N., Dehal, P. S. & Arkin, A. P. FastTree 2 - Approximately maximum-likelihood trees for large alignments. *PLoS One* **5**, (2010).
77. Moore, R. M., Harrison, A. O., McAllister, S. M., Polson, S. W. & Wommack, K. E. Iroki: automatic customization and visualization of phylogenetic trees. *PeerJ* **8**, e8584 (2020).
78. Gibson, M. I., Chen, P. Y. T. & Drennan, C. L. A structural phylogeny for understanding 2-oxoacid oxidoreductase function. *Curr. Opin. Struct. Biol.* **41**, 54–61 (2016).
79. Price, M. N. & Arkin, A. P. PaperBLAST: Text Mining Papers for Information about Homologs. *mSystems* **2**, 1–10 (2017).
80. Paradis, E. & Schliep, K. Ape 5.0: An environment for modern phylogenetics and evolutionary analyses in R. *Bioinformatics* **35**, 526–528 (2019).
81. Letunic, I. & Bork, P. Interactive Tree of Life (iTOL) v4: Recent updates and new developments. *Nucleic Acids Res.* **47**, 256–259 (2019).
82. Coursolle, D., Baron, D. B., Bond, D. R. & Gralnick, J. A. The Mtr respiratory pathway is essential for reducing flavins and electrodes in Shewanella oneidensis. *J. Bacteriol.* **192**, 467–474 (2010).
83. Coursolle, D. & Gralnick, J. A. Modularity of the mtr respiratory pathway of shewanella oneidensis strain MR-1. *Mol. Microbiol.* **77**, 995–1008 (2010).
84. Gupta, D. *et al.* Photoferrotrophs produce a PioAB electron conduit for extracellular electron uptake. *MBio* **10**, 1659–1677 (2019).
85. Jiao, Y. & Newman, D. K. The pio operon is essential for phototrophic Fe(II) oxidation in Rhodopseudomonas palustris TIE-1. *J. Bacteriol.* **189**, 1765–1773 (2007).
86. Liu, J. *et al.* Identification and characterization of MtoA: A decaheme c-type cytochrome of the neutrophilic Fe(ll)-oxidizing bacterium Sideroxydans lithotrophicus ES-1. *Front. Microbiol.* **3**, 1–11 (2012).
87. Gralnick, J. A., Vali, H., Lies, D. P. & Newman, D. K. Extracellular respiration of dimethyl sulfoxide by Shewanella oneidensis strain MR-1. *Proc. Natl. Acad. Sci. U. S. A.* **103**, 4669–4674 (2006).
88. Jiménez Otero, F., Chan, C. H. & Bond, D. R. Identification of Different Putative Outer Membrane Electron Conduits Necessary for Fe(III) Citrate, Fe(III) Oxide, Mn(IV) Oxide, or Electrode Reduction by Geobacter sulfurreducens. *J. Bacteriol.* **200**, 1–20 (2018).